A new simple approach to prepare rare-earth metals-modified TiO$_2$ nanotube arrays photoactive under visible light: Surface properties and mechanism investigation

Patrycja Parnicka[a], Paweł Mazierski[a,*], Wojciech Lisowski[b], Tomasz Klimczuk[c], Joanna Nadolna[a], Adriana Zaleska-Medynska[a]

[a] Department of Environmental Technology, University of Gdansk, 80-308 Gdansk, Poland
[b] Institute of Physical Chemistry, Polish Academy of Sciences, 01-224 Warsaw, Poland
[c] Department of Solid State Physics, Faculty of Applied Physics and Mathematics, Gdansk University of Technology, 80-233 Gdansk, Poland

ARTICLE INFO

ABSTRACT

Application of Ti$_{90}$RE$_{10}$ alloys (RE = Ho, Er, Nd, Y, Ce, Tm) as a working electrode, instead of Ti pure foil in anodic oxidation in a fluoride-based electrolyte, resulted in formation of well-ordered nanotubes made of TiO$_2$ and RE$_2$O$_3$ mixture, which could be efficiently used for pollutant removal from water and air phase upon UV and visible irradiation and easily separable from the reaction mixture to recycle. The as-prepared NTs were characterized by scanning electron microscopy (SEM), energy-dispersive spectroscopy (EDX), diffuse reflectance spectroscopy (DRS), luminescence spectroscopy, X-ray diffraction (XRD), and X-ray photoelectron spectroscopy (XPS). The photocatalytic activity of the synthesized samples was investigated used phenol and toluene as a model compounds to follow degradation kinetics. The influence of the RE metals on the photoelectrochemical performance of modified TiO$_2$ NTs was investigated. Surface morphology analysis showed formation of uniform and vertically oriented NTs structures with an open tube top and smooth walls. The results of EDX, XRD and XPS analysis proved that RE ions exist as surface compounds (RE^{3+} oxides). Visible light induced photoactivity (both photocatalytic and photoelectrochemical) is mostly pronounced in the presence of nanotubes obtained by anodic oxidation of Ti$_{90}$Ho$_{10}$ alloy. These nanotubes are able to degrade toluene in the gas phase even by irradiation of low-powered light source, such as light emitting diodes (λ_{max} = 465 nm). Photocatalytic test of phenol degradation in the presence of scavenger indicates that photogenerated electrons and superoxide radicals play a meaningful role in the photocatalytic degradation of pollutants under visible irradiation. In addition, the photoelectrochemical tests performed under the influence of visible light irradiation confirmed that the RE-modification of TiO$_2$ NTs caused a significant increase of photocurrent (up to 10 times higher). The new and original results on the preparation of RE$_2$O$_3$/TiO$_2$ nanotubes obtained in one step anodic oxidation and photocatalytic activity in aqueous and gas phases represent an important contribution then will benefit photocatalytic surfaces preparation technologies.

Introduction

In recent years the one-dimensional nanostructures (such as nanofiber, nanorods, nanotube, and nanowires) have attracted significant interest due to their high surface-to-volume ratios and directional shapes, which exhibits enhanced photoelectrochemical properties [1–3]. Belong to them – high electron mobility or quantum confinement effects, low dimensionality, a very high specific surface area, and better adsorption ability [4–6].

Especially interesting is the formation of nanotubes (NTs) on various alloys by the electrochemical anodization process (relatively straightforward and cost-effective technique). This process mainly employs titanium alloy in order to obtain self-organized titanium dioxide-based nanotube layers. This approach results in a combination of their unusual physical properties with a well controllable nanotubular structure [7]. TiO$_2$ nanotubes from a wide range of applications could be used as a photocatalytic material [8], in solar cells [9], in electrochromic devices [10], as a biomedical coating [11], drug-delivery capsule [12], and as biosensors [13]. The photocatalytic application plays an important role due to growing problem with environment

pollutants and TiO_2 can be used for the treatment of wasted water [14,15] and polluted air [16,17].

Application of solar light to drive pollutants degradation over semiconductor surface is one of the green approaches proposed for air, water and wastewater treatment. Thus, a lot of attention is paid to different methodologies improve TiO_2 properties in visible range of electromagnetic spectrum because it allows obtaining photocatalysts active under solar light, and at the same time trying to retain its high stability and high quantum field. Several reports have shown that these requirements can be met by rare earth (RE) modification of TiO_2 [14,18,19]. In the literature, the most often presented preparation routes of RE-TiO_2 nanotubes have been one- or two-step electrochemical anodization process. Generally, the one-step method consists in anodization of titanium foil in ethylene glycol-based electrolyte containing RE precursor [20,21]. While, two-step method consists of anodic oxidation of Ti (in the first step) followed by electrochemical doping from electrolyte (in the second step) [22,23]. However, despite the widely described the growth of nanotubes on various binary alloys (for example, TiNi, TiMn, TiCr, TiZr, TiAl, TiMo, TiNb [24–32] there is no information about growing nanotubes from suitable TiRE alloys. Alloys anodization thus enables the growth of mixed anodic oxides with tailored and improved properties for a wide range of applications [33].

Recently, it was reported that TiO_2 modification with Ho [23], Er [34], Nd [18], Y [35], Ce [36], Tm [37] can enhance the photocatalytic activity both under UV and visible irradiation. Contrary to previously reported RE_2O_3-TiO_2 nanotubes, obtained by two-step electrochemical method [23], currently presented method allows to form photocatalytic surface in one step reaction, which is less time-consuming method and avoids to generate spend electrolyte containing lanthanides ions. Therefore, the presented research is a promising way to adoption and implementation of the principles of green technology (consisting in minimization of energy and materials input as well as reducing waste generation) [38].

In view of this, RE-TiO_2 NT arrays were prepared by the anodization of $Ti_{90}RE_{10}$ (RE = Ho, Er, Nd, Y, Ce, Tm) alloys for the first time and their properties were discussed in detail. The photocatalytic activity and stability of all of obtained photocatalysts were evaluated by monitoring the degradation of phenol and toluene as water and air pollution models, respectively. To provide insight into which reactive species participating in the degradation mechanism, a test with scavengers was also performed. The influence of the RE metals on the photoelectrochemical performance of modified TiO_2 NTs was investigated as well.

Experimental

Materials

A titanium foil and TiRE alloys with 10 wt% of rare earth metal content (0.5 mm thickness, 99.7% purity, HMW-Hauner Metallische Werkstoffe Röttenbach, Germany) was cut into pieces of 25×25 mm. Acetone, isopropanol, methanol, ammonium oxalate and silver nitrate were purchased from POCh S.A (Poland), benzoquinone, phenol and *tert*-butanol were bought from Sigma-Aldrich, ethylene glycol was acquired from CHEMPUR (Poland), and ammonium fluoride was bought from Acros Organic (Belgium). Deionized (DI) water with a conductivity of 0.05 μS was used to prepare all of the aqueous solutions.

Preparation of pristine TiO_2 and RE-TiO_2 nanotube arrays

Pristine TiO_2 and RE-TiO_2 NT arrays were fabricated by electrochemical anodization of Ti foil and TiRE (10 wt% RE) alloys with dimensions of 25×25 mm. Prior to anodizing samples were ultrasonically cleaned with acetone, isopropanol, methanol and deionized water for 10 min (in each solvent). The anodization was carried out in an electrolyte solution containing ethylene glycol, deionized water

(2 vol%) and ammonium fluoride (0.09 M) and using the Ti or TiRE substrates as an anode and a cylindrical platinum grid as a cathode, applying a constant voltage (40 V) at room temperature for 1 h. The Ag/AgCl reference electrode was used to control the process and obtain information about the actual working electrode potential. To measure the actual current and potential of anode versus Ag/AgCl, a reference electrode digital multimeter (BRYMEN BM857a) was applied. After anodization, the initial layer was removed by sample ultrasonication in the deionized water for 5 min and then dried in air at 80 °C for 24 h. Finally, the samples were annealed at 450 °C in air (heating rate: 2 °C/min) for 1 h in order to obtain anatase crystalline structure.

Characterization techniques

The morphology and microstructure of the anodized samples were characterized by field emission scanning electron microscopy (FE-SEM, JSM-7610F, JEOL). The UV–Vis absorbance spectra of obtain nanotubes were recorded on Shimadzu UV–Vis Spectrophotometer (UV 2600) equipped with an integrating sphere. The baseline was determined using barium sulphate as a reference. The spectra were registered in range of 300 to 800 nm, with a scanning speed of 250 nm/min at the room temperature. The photoluminescence (PL) spectra were recorded by LS-50B Luminescence Spectrometer equipped with a Xenon discharge lamp and a R928 photomultiplier. The excitation radiation (300 nm) was directed onto the surface of the samples at an angle of 90°. X-ray diffraction method (PANalyticalX'Pert Pro, Cu-Kα radiation) was used to check chemical composition of the samples. The data were collected for $10° < 2\Theta < 70°$ range, with a step of 0.02°. The diffraction patterns were analyzed by the LeBail profile refinement method using HighScore Plus program. X-ray photoelectron spectroscopy measurements were performed using a PHI 5000 VersaProbe (ULVAC-PHI) spectrometer with monochromatic Al Kα radiation (hν = 1486.6 eV) from an X-ray source operating at 25 W and 15 kV and a 100 μm spot size. High-resolution (HR) XPS spectra were collected with a hemispherical analyser at a pass energy of 23.5 eV, an energy step size of 0.075–0.1 eV and a photoelectron take-off angle of 45° with respect to the surface plane. CasaXPS software (version 2.3.18) was used to evaluate the XPS data. The binding energy (BE) scale of all detected spectra was referenced by setting the BE of the aliphatic carbon peak (C–C) signal to 284.8 eV.

Measurement of photocatalytic activity

The photocatalytic activity of pristine and RE-modified TiO_2 NTs was evaluated with phenol and toluene as water and air pollution models, accordingly. The photodegradation experiment of phenol in the presence of NTs under UV–Vis or visible light irradiation were performed using a 1000 W Xenon lamp (Oriel 66021) with equipped with water IR cut-off filter and optical filters (GG350 or GG420) to cut-off the emission below 350 or 420 nm. Generally, a phenol solution (8 mL, 0.21 mM) in quartz photoreactor was mixed (550 rpm) and aerated (5 dm³/h) in the dark for 30 min in order to establish an adsorption-desorption equilibrium between phenol and photocatalyst. Immediately after, the photoreactor was irradiated with a cut-off spectrum of light. Samples of a 0.5 mL reaction mixture were collected at regular time periods during irradiation and 20 μL of them were examined by Shimadzu high-performance liquid chromatography. The HPLC system was equipped with a C-18 column (Kinetex, 150 mm × 3 mm; particle size of 2.6 μm; pore diameter 100 Å) and the mobile phase was composed of a mixture of water and 0.1% formic acid using isocratic elution (80/20 v/v) with a constant flow rate equal to 0.4 mL/min. The SPD-M20 A diode detector was fixed at λ = 205 nm. To investigate the mineralization of phenol, the total organic carbon (TOC) was carried using TOC analyzer Shimadzu TOC-L. In addition, the research was extended to include which reactive individuals participate in the phenol degradation mechanism under visible (λ > 420 nm) light irradiation.

These studies included a hydroxyl radical test using terephthalic acid (0.5 mM) and a reactive species formation test using benzoquinone, silver nitrate, ammonium oxalate and *tert*-butanol (solution of scavenger and phenol 1/1C/C) as scavengers were carried out. The efficiency of hydroxyl radical generation was measured using a Perkin Elmer limited LS50B spectrophotometer equipped with a xenon discharge lamp and an R928 photomultiplier. The obtained solution was measured with an excitation wavelength of 315 nm. The photodegradation experiment of toluene in the presence of NTs was performed under the influence of radiation emitted by light-emitting diodes (LEDs) with λ_{max} = 375, 415 and 465 nm. The reactions were carried in a flat stainless steel photoreactor equipped with a quartz window, two valves, and a septum. After the gaseous mixture (200 ppm, flow rate: 0.3 dm^3/min) was passed through the reaction chamber for 1 min and establishing an adsorption-desorption equilibrium (30 min in dark) the illumination was initialized. 200 μL samples were withdrawn regularly from the reactor for analysis. The toluene concentration was analysed by a Thermo Scientific gas chromatography (Trace 1300) equipped with an Elite-5 capillary column and a flame ionization detector.

Measurement of photoelectrochemical properties

The photoelectrochemical properties of pristine and modified TiO$_2$ NTs were investigated using an AutoLab PGSTAT 204 potentionstat-galvanostat (Methrom Autolab) in the three-electrode system. Pristine and modified TiO$_2$ NTs were used as a working electrode, Ag/AgCl/ 0.1 M KCl and Pt mesh as reference and counter electrodes, respectively. Prior to measurement, electrolyte (0.5 M Na$_2$SO$_4$ water solution) was purged with argon for 1 h. The photoelectrochemical properties of prepared samples under UV–Vis and visible irradiation were performed using a 150 W Xenon lamp (Hamamatsu Photonics K.K., model E7536) with equipped with water IR cut-off filter and optical filters (GG420) to cut-off the emission below 420 nm. The irradiation intensity was measured by an optical power meter (Hamamatsu, C9536-01) and was adjusted to 4 mW/cm^2 for visible irradiation.

Results and discussion

Surface morphology and growth mechanism

The growth of the nanotubular oxide can be monitored by recording the current density-time characteristics. Fig. 1 shows the current transients (j-t curves) recorded during holding the sample in a 0.09 M

fluoride-containing ethylene glycol electrolyte. The formation of RE-TiO$_2$ NTs includes a competition between electrochemical etching and chemical dissolution processes. The graph shows the classical anodization curve shape. The registered i-t curves of all samples are similar and present typical III-stage curve described previously in the literature [39–41] and clearly suggests the formation of nanotubes from TiRE alloys (10 wt% RE). In the initial stage of anodization (0–100 s), the compact TiO$_2$ layer is formed on the Ti surface which causes rapid drop in the current density. Subsequently, as light increase in current density is observed because oxide layer is attacked by fluoride ions and pores begin to grow. In the final stage (from approximately 1000 s to 3600 s), a steady-state formation of nanotubular oxide is observed. In other words, the current density remains unchanged due to dynamic equilibrium between the growth and the dissolution of TiO$_2$ nanotubes (formation of TiF$_6^{2-}$). Concluding, it is likely that TiRE alloys do not affect the chemical properties (solubility of the oxide in fluoride, the formation of TiF$_6^{2-}$ complex) and preferred nanotubular morphology is completely retained (what will be described and proved later).

Figs. 2 and S1 (see supplementary material) presents top views and cross-sectional morphologies of synthesized RE-modified and pristine TiO$_2$ NTs, respectively. It shows that the anodization of Ti$_{90}$RE$_{10}$ alloys at a relatively high voltage (40 V) in an electrolyte solution containing ethylene glycol, deionized water (2 vol%) and ammonium fluoride (0.09 M) for 1 h and annealed in 450 °C for 1 h with heating rate 2 °C/ min resulted in the formation of uniform and vertically oriented NTs structures with an open tube top and smooth walls. Literature review indicates that a small amount of the H$_2$O in the electrolyte leads to the formation of highly ordered TiO$_2$-based NTs. In contrast, the excessive H$_2$O content results in disordered structure due to quick dissolution of the NTs during anodization [42]. Based on these studies, the amount of water in the electrolyte was selected.

The tubes dimensions including diameter, length and wall thickness, based on SEM images are given in Table 1. RE-TiO$_2$ NTs had the similar external diameter and wall thickness and were determined to 97 ± 2 nm and 18 ± 1 nm, respectively. The length of tubes was varied in the range from 4.5 to 5.6 μm. The developed surface area of RE-modified TiO$_2$ NTs was calculated, and all of the sample's values amounted from 2251·10^3 to 2821·10^3 nm^2.

Changes in the surface area is a consequence of slight differences in geometrical dimensions. Moreover, a large surface area is often considered to be advantageous for the photocatalytic reactions [44]. Based on our previous paper [43], in order to explore the general NT forming principles for other Ti alloys, the pristine TiO$_2$ NTs samples were prepared under different conditions (30, 40, 50 V for 1 h) using Ti sheets. Pristine NTs presented an average length of 1.5–6 μm, a tube diameter of 70–120 nm, and a wall thickness of 10–18 nm [43]. It is well known that nanotubes dimensions are strongly dependent on the anodization potential, namely, they are increased by increasing the applied voltage while the anodic oxidation processes [45]. In comparison to RE-TiO2 NTs, the pristine TiO$_2$ NTs synthesised at a voltage of 40 V presented a different morphology, i.e. the sample was characterized by lower geometrical dimensions. Madian et al. [46] observed that the wall thicknesses of NTs grow directly proportional to Sn contents in Ti-Sn alloys. Yasuda et al. and Miangar et al. [27,47] have reported that the main reason for increasing NT dimensions is due to the different standard enthalpies of formation of TiO$_2$ and ZrO$_2$, also the equilibrium constant of (NH$_4$)$_2$[TiF$_6$] is lower than that of (NH$_4$)$_2$ [ZrF$_6$] thus NTs were characterized by different length. That suggested that RE metals in TiRE alloys can also change the growth kinetics of the nanotube. In other hand, Kim et al. [48] research demonstrated that the diameter of the NTs, was not dependent on Zr content in TiZr alloys, however, it influenced to the interspace between the TiO$_2$ nanotubes. When the Zr content was 10 wt%, the interspace was the smallest, while when Zr content increased the interspace between the NTs had increasing. These studies have shown that ZrO$_2$ has a role in the formation of NTs on the surface. This these may also be consistent with our observations. In
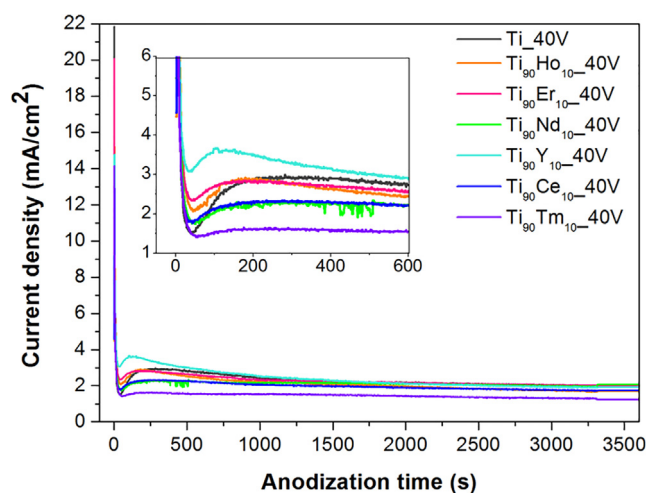

Fig. 1. Current density-time curves recorded for the anodization of Ti sheet and Ti/RE alloys at a constant voltage of 40 V during 1 h in a fluoride-containing ethylene glycol electrolyte.
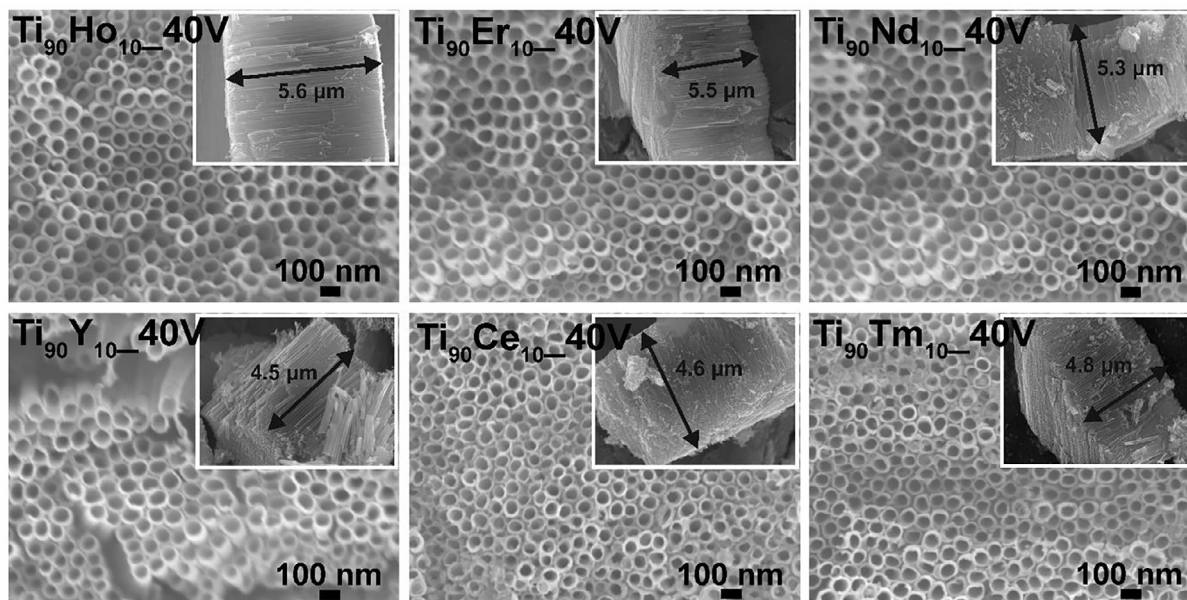
Fig. 2. Top views and cross-sectional morphologies of RE-TiO$_2$ NTs.

order to confirm this explanation, the energy-dispersive spectrometer analysis was conducted and exhibited the presence of titanium, oxygen and rare earth atoms in the compositions of prepared samples. The EDX mapping images (Fig. 3) demonstrated that RE elements were uniformly distributed on the surface of the TiO$_2$ NTs. Nevertheless, the Ti$_{90}$Y$_{10}$ alloy exhibits less homogeneous distribution of yttrium across the substrate and also agglomerates of yttrium are observed in some areas.

Optical and luminescence properties

To examine the optical absorption properties of obtaining NTs, the UV–Vis diffuse reflectance spectra were investigated, and data were converted by Kubelka-Munk (K-M) function to obtain absorption spectra. Obtained data are shown in Fig. 4. The typical absorption band in the UV region and the broad band in the range of 390–800 nm were clearly observed for all nanotubes. The absorption has assigned to produced holes trapped at lattice oxide ions immediately below the surface and electrons trapped in the bulk at Ti^{3+} center [49]. The RE-TiO$_2$ samples exhibited wider absorption range than that of TiO$_2$ due to the RE modification. As shown, there is an apparent absorption peak from ~400 to ~700 nm from the RE-O-Ti NTs. RE could lead to the formation of the additional transitions between the different energy levels of oxygen vacancy, Ti^{3+}, and conduction band. However, absorption bands in the visible region from RE^{3+} ions were not detected because of broad band attributed to pristine TiO$_2$ NTs.

Although numerous factors may be responsible for the photocatalytic activity, the intense investigations of photoluminescence

spectroscopy were applied to understand the rate of electron-hole recombination, determining the presence of surface defects, trap states, and sub-band states in the mid-gap level of photocatalysts [2,3]. Fig. 5 shows photoluminescence spectra of all samples. The shapes of the spectra were similar for all NTs, and emission and position peaks were observed among all series. According to the available literature [49–51], the intense blue emission at 425 nm can be attributed to the existence of self-trapped excitons from TiO$_6$$^{8-}$ octahedron. In turn, peaks of approximately 445 and 480 nm could be originated to the oxygen vacancies, which can form intermediate energy states located below the conduction band and are able to trap electrons. The least intense peaks approximately 525 nm is most likely resulted from the recombination of electrons in oxygen vacancies related luminescent centers to the holes in the valence band of TiO$_2$ [49–51]. Additionally, the RE-modified TiO$_2$ NTs exhibited the higher photoluminescence intensity than TiO$_2$ NTs. A probable reason is the occurrence of numerous RE-O-Ti bonds increasing the presence of surface or structural defects, which can improve the photocatalytic performance [52].

X-ray diffraction studies

Fig. 6 presents X-ray diffraction patterns for the whole series of studied samples. A pattern for the pristine sample shows only TiO$_2$ (anatase) and Ti metal for which phases the Bragg reflections are marked by red and green bars, respectively. The Miller indices for anatase are also presented. The intensity of the highest peak of anatase (1 0 1) is comparable to the highest peak of titanium (1 0 1), latter observed at 2Θ = 40.2°.

Table 1
Sample labels, characterization and photocatalytic activity of TiO$_2$ and RE-TiO$_2$ nanotubes.

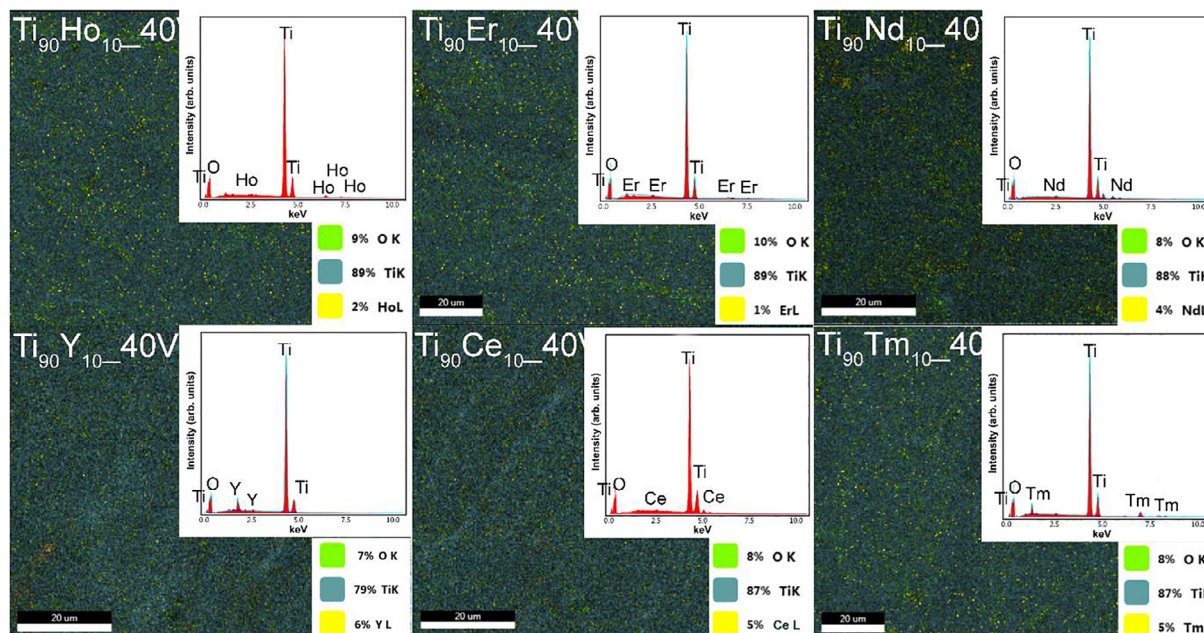| Samples label	Modification type	External diameter (nm)	Nanotubes length (μm)	Wall thickness (nm)	Reference
Ti_30V	None	80	1.5	10	Our previous work [43]
Ti_40V	None	100	3.0	13	
Ti_50V	None	120	6.0	18	
Ti$_{90}$Ho$_{10}$_40V	Ho	99	5.6	19	This work
Ti$_{90}$Er$_{10}$_40V	Er	98	5.5	19	
Ti$_{90}$Nd$_{10}$_40V	Nd	98	5.3	18	
Ti$_{90}$Y$_{10}$_40V	Y	98	4.5	18	
Ti$_{90}$Ce$_{10}$_40V	Ce	96	4.6	17	
Ti$_{90}$Tm$_{10}$_40V	Tm	95	4.8	17	

Fig. 3. The EDX spectrum of complete element distribution.
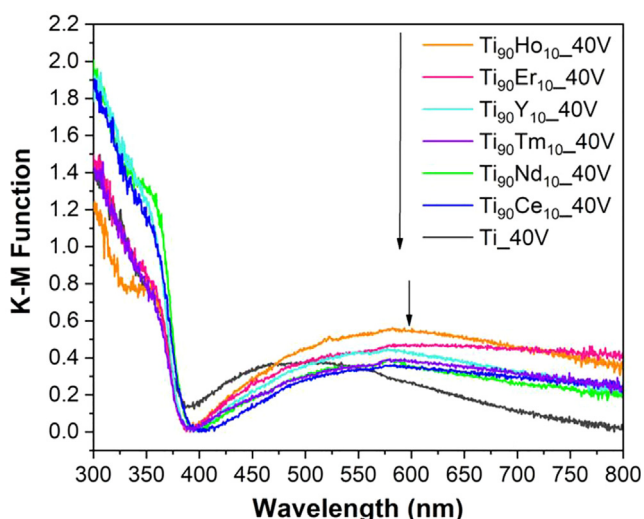
Fig. 4. UV–Vis Kubelka-Munk absorption of TiO_2 and RE-modified TiO_2 nanotubes.

Fig. 5. Photoluminescence spectra of TiO_2 and RE-modified TiO_2 nanotubes.

X-ray patterns for RE-TiO$_2$ samples reveal the same majority phases – TiO$_2$, Ti, however additional reflections are also seen. For Y-TiO$_2$ and Nd-TiO$_2$ oxyfluorides (YOF and NdOF) were found which is in agreement with the highest fluorine concentration in those samples as it is discussed in 3.4. YOF and NdOF form in a regular (Fm-3m, s.g. #225) and a tetragonal crystal structure (P4/nmmm, s.g. 129), respectively. X-ray diffraction reflections for both phases are represented by blue bars (the lowest set of bars). For Ce-TiO$_2$ and heavier rare earth metals (Ho, Er, Tm) RE$_2$O$_3$ (Ia3, s.g. #206) oxide was found and the strongest reflection (2 2 2) at approximately 29.5 deg. is marked by a vertical arrow. Besides Ce$_2$O$_3$, CeO$_2$ (marked by green arrows) is also present in agreement with XPS results.

LeBail method was used for refining lattice parameters for Ti and iO$_2$. The averaged crystallite size for the anatase was calculated using the Scherrer formula. Obtained results are shown in Table 2. As expected, the lattice parameters for Ti metal foil are smaller than for TiRE foils. This is likely caused by the fact that TiRE foil contains 10% of RE metal. There is no obvious trend visible for the anatase, i.e. the
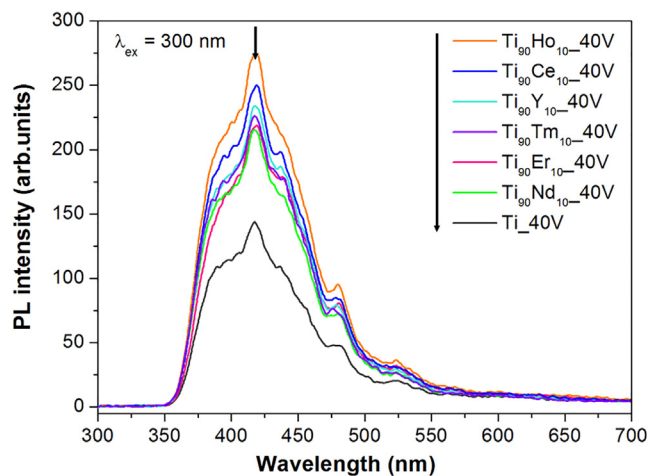
estimated lattice parameters do not shrink for heavier RE. Lack of this effect as well as no observed shift of (1 0 1) diffraction peaks suggests that the rare earth metals do not incorporate into the anatase crystal structure substituting titanium metal, they are located on the surface of nanotubes in the form of oxides.

Chemical composition

The elemental composition (in at.%) in the surface layer of pristine TiO2 and RE (Nd, Ce, Tm, Ho, Er, Y) modified TiO2 NTs was evaluated by XPS. The analysis was performed for each of samples on three areas (250 μm × 250 μm) separated by about 3 mm. The average data from these measurements are shown in Table 3 and all atomic composition data are collected in supplementary material in Table S1.

The presented data confirm the effective modification of the RE and reveal their different surface contribution. The surface compositions of Nd, Ce and Tm are close to those expected in Ti$_{90}$RE$_{10}$ alloys formation. However, the Ho and Er atomic content was found to be smaller and the Y much larger than expected (see RE/Ti ratios in Table 3). Carbon, nitrogen and fluorine species were also detected in the surface region of all samples (Table 3). They are common contaminants of TiO$_2$
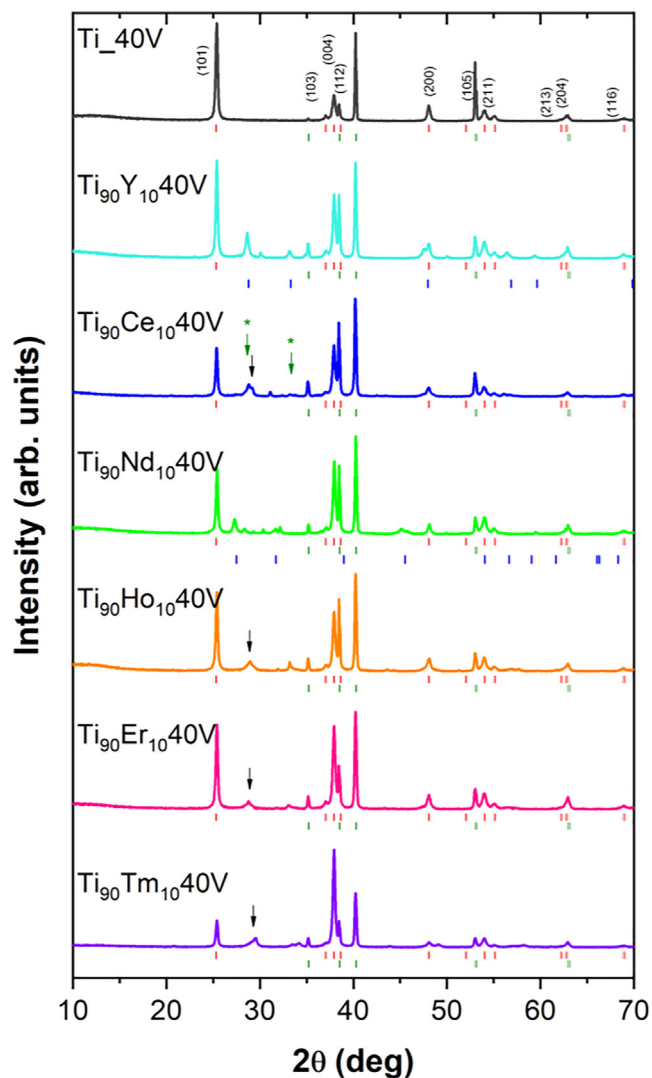
Fig. 6. X-ray diffraction patterns for all studied samples. Red and green bars represent Bragg reflections for Ti and TiO_2 (anatase), respectively. Miller indices for the anatase are provided. Oxyfluorides, YOF and NdOF are marked by blue bars. Vertical arrows show the strongest (2 2 2) reflection for RE_2O_3 oxide, and in addition two reflections for CeO_2 are marked by green stars. (For interpretation of the references to colour in this figure legend, the reader is referred to the web version of this article.)

Table 2
Unit cell parameters of TiO_2 and RE-modified TiO_2 nanotubes.

Samples label	Anatase			Ti	
	a (Å)	c (Å)	d (Å)	a (Å)	c (Å)
Ti_40V	3.7919(3)	9.5148(7)	340	2.9564(2)	4.6908(2)
Ti$_{90}$Y$_{10}$_40V	3.8001(9)	9.523(2)	310	2.9596(5)	4.6975(8)
Ti$_{90}$Ce$_{10}$_40V	3.7947(6)	9.517(1)	350	2.9573(3)	4.6935(5)
Ti$_{90}$Nd$_{10}$_40V	3.7925(7)	9.517(1)	310	2.9561(4)	4.6922(7)
Ti$_{90}$Ho$_{10}$_40V	3.7948(7)	9.518(1)	300	2.9572(4)	4.6928(6)
Ti$_{90}$Er$_{10}$_40V	3.7952(4)	9.5208(9)	330	2.9579(2)	4.6951(4)
Ti$_{90}$Tm$_{10}$_40V	3.7925(7)	9.521(1)	370	2.9573(4)	4.6939(7)

nanotubes obtained by anodic oxidation, and all derive from the electrolyte [53,54]. The chemical character of the elements originating from pristine TiO_2 (Ti, O) and from all RE detected within the surface layer of the RE-TiO_2 nanotubes were identified from the HR XPS spectra showed in Fig. 7 and summarized in Table S1.

The Ti 2p spectrum is resolved into two doublet-components at

Table 3
Elemental composition (in at. %) in the surface layer of RE (Nd, Ce, Tm, Ho, Er, Y) modified Ti$_{90}$RE$_{10}$ NTs, evaluated by XPS. The analysis were performed for each of samples on three areas (250 μm x250 μm) separated by about 3 mm. The average data from these measurements are shown in the table.

| Sample label	Elemental composition (at%)											RE/Ti ratio
	Ti	O	C	F	N	Nd	Ce	Tm	Ho	Er	Y	
Ti_40V	23.74 ± 0.92	62.05 ± 1.11	13.09 ± 2.02	0.82 ± 0.27	0.28 ± 0.08	–	–	–	–	–	–	0
Ti$_{90}$Nd$_{10}$_40V	22.20 ± 1.62	59.95 ± 2.14	12.66 ± 3.83	2.79 ± 0.69	0.24 ± 0.07	2.16 ± 0.35	–	–	–	–	–	0.098
Ti$_{90}$Ce$_{10}$_40V	24.43 ± 0.75	66.95 ± 0.92	5.42 ± 1.19	0.98 ± 0.11	0.32 ± 0.08	–	1.91 ± 0.32	–	–	–	–	0.078
Ti$_{90}$Tm$_{10}$_40V	20.76 ± 0.70	61.07 ± 0.59	14.73 ± 0.56	1.54 ± 0.15	0.34 ± 0.25	–	–	1.55 ± 0.28	–	–	–	0.075
Ti$_{90}$Ho$_{10}$_40V	22.14 ± 1.20	59.72 ± 1.87	16.39 ± 3.11	0.76 ± 0.12	0.34 ± 0.16	–	–	–	0.66 ± 0.11	–	–	0.030
Ti$_{90}$Er$_{10}$_40V	24.45 ± 0.10	64.96 ± 0.38	8.06 ± 0.58	1.50 ± 0.11	0.17 ± 0.11	–	–	–	–	0.86 ± 0.03	–	0.035
Ti$_{90}$Y$_{10}$_40V	15.20 ± 5.38	56.60 ± 5.83	13.14 ± 3.64	4.87 ± 3.29	–	–	–	–	–	–	10.20 ± 4.30	0.671
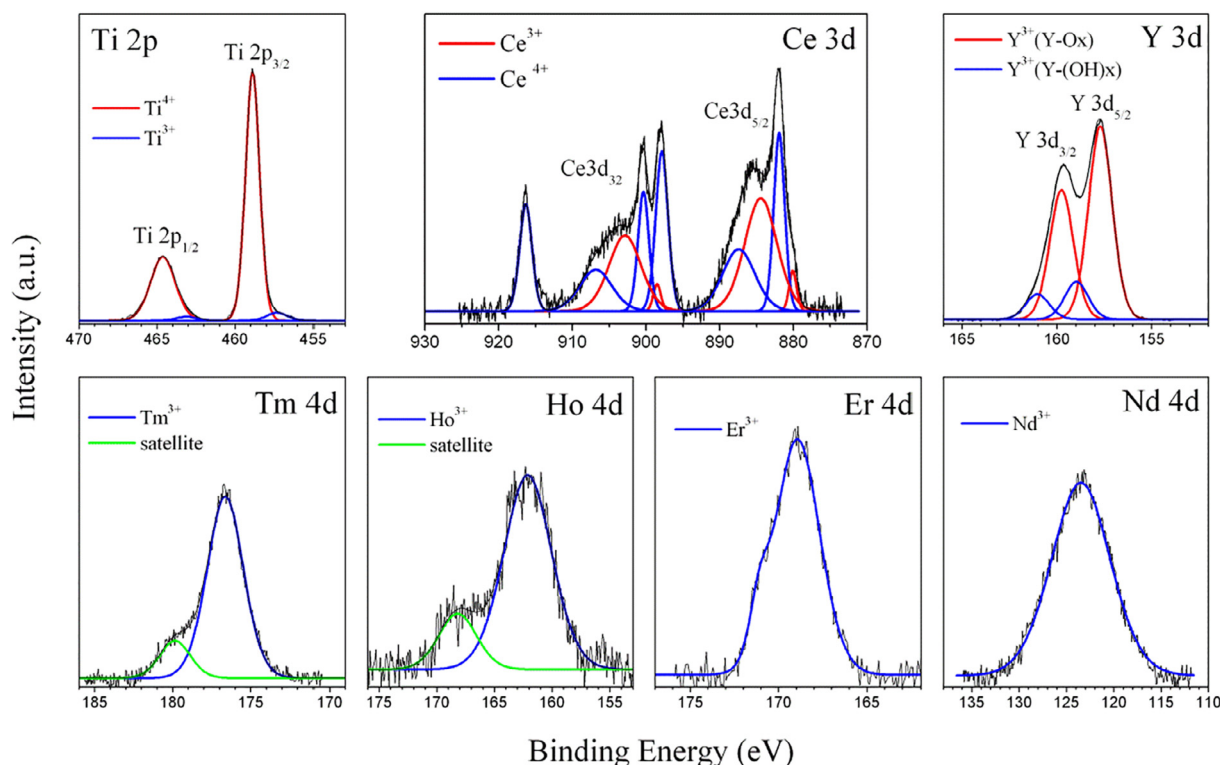
Fig. 7. XPS spectra of RE-modified TiO$_2$ NTs.

Table 4
Photocatalytic activity of TiO$_2$ and RE-TiO$_2$ nanotubes.

Samples label	Phenol degradation rate, r (μmol·dm^{-3}·min^{-1})		Toluene degradation rate, r (μmol·min^{-1}) $\times 10^3$		
	UV–Vis, $\lambda > 350$ nm	Vis, $\lambda > 420$ nm	$\lambda_{max} = 375$ nm	$\lambda_{max} = 415$ nm	$\lambda_{max} = 465$ nm
Ti_30V	1.25	0.04	4.75	0.52	0.13
Ti_40V	1.35	0.13	4.93	0.62	0.16
Ti_50V	1.44	0.15	4.70	0.72	0.24
Ti$_{90}$Ho$_{10}$_40V	2.37	0.45	5.21	2.87	2.24
Ti$_{90}$Er$_{10}$_40V	1.82	0.43	5.16	2.85	1.82
Ti$_{90}$Nd$_{10}$_40V	3.04	0.40	5.13	1.87	1.70
Ti$_{90}$Y$_{10}$_40V	2.12	0.13	5.13	2.34	1.37
Ti$_{90}$Ce$_{10}$_40V	3.09	< detection limit	5.15	< detection limit	< detection limit
Ti$_{90}$Tm$_{10}$_40V	2.96	0.26	5.14	1.20	0.81

binding energies of Ti 2p$_{3/2}$ signal at 458.6 and 457.3 eV and are assigned to Ti^{4+} and Ti^{3+}, respectively. The Ti^{4+} is the dominant surface state and relative contribution of the Ti^{3+} species is similar for all Ti$_{90}$RE$_{10}$ NTs (3.6–4.9%) (Table S2). The deconvolution of the Ce 3d spectrum (Fig. 7) reveals five doublets formed by 3d$_{5/2}$ and 3d$_{3/2}$ spin-orbit splitting components, separated by 18.4 $\pm$ 0.2 eV [55–58]. The Ce 3d$_{5/2}$ peaks at BE of 880.1 eV and 884.4 eV are related to Ce^{3+} species while the corresponding peaks at 882.0 eV, 887.5 eV and 897.9 eV are assigned to Ce^{4+} species [57,58]. All deconvoluted peaks were used to determine the relative contribution of the Ce^{3+} and Ce^{4+} states at the surface to be 41.9% and 58.4%, respectively (Table S2). The Y 3d spectrum reveals two states of Y^{3+} surface species represented by Y3d$_{5/2}$ signals at 157.9 eV and 159, 2 eV. First, one can be attributed to oxide (Y-Ox) and second to hydroxide (Y-OH) groups [59–61]. The Tm 4d, Ho 4d, Er 4d and Nd 4d peak positions located at 176.6 eV, 162.0 eV, 168.7 eV, and 123.2 eV, respectively (Fig. 7), indicate that RE surface compounds can be attributed to RE^{3+} oxides, namely Tm$_2$O$_3$ [59,62], Ho$_2$O$_3$ [59,60,63], Er$_2$O$_3$ [59,60,64] and Nd$_2$O$_3$ [65,66]. The Tm 4d and Ho 4d peaks are accompanied by satellites at BEs 180.0 and 167.0 eV, respectively. The XPS results demonstrated the RE oxides are distributed on the surface of TiO$_2$ NTs, which is in good agreement with

the XRD and EDX results.

Photocatalytic performance and mechanism discussion

Definitely, the most attended application of titania-based photocatalysts is the photodegradation of various organic pollutants. In order to evaluate the photocatalytic activity and stability of the obtained NTs, phenol and toluene were employed as target pollutants. Phenol and toluene as organic compounds are commonly present in the environment and human surroundings that reveal toxic influence towards living organisms [67,68]. The photodegradation reaction in aqueous solution was conducted under influence of UV–Vis ($\lambda > 350$ nm) and visible ($\lambda > 420$ nm) light irradiation, while the reactions in gas phase were illumination by light-emitting diodes (LEDs) with $\lambda_{max} = 375$, 415 and 465 nm. The observed degradation rates (calculated for the 60 min of irradiation) are listed in Table 4.

The highest phenol degradation rate under UV–Vis irradiation (Fig. 8a), were observed for the samples obtained from Ti$_{90}$Ce$_{10}$, Ti$_{90}$Nd$_{10}$, Ti$_{90}$Tm$_{10}$ alloys (3.09, 3.04, and 2.96 μmol·dm^{-3}·min^{-1}, respectively). It should be noted that remaining samples showed considerably higher reaction rate than pristine TiO$_2$ NTs. Substantially, the
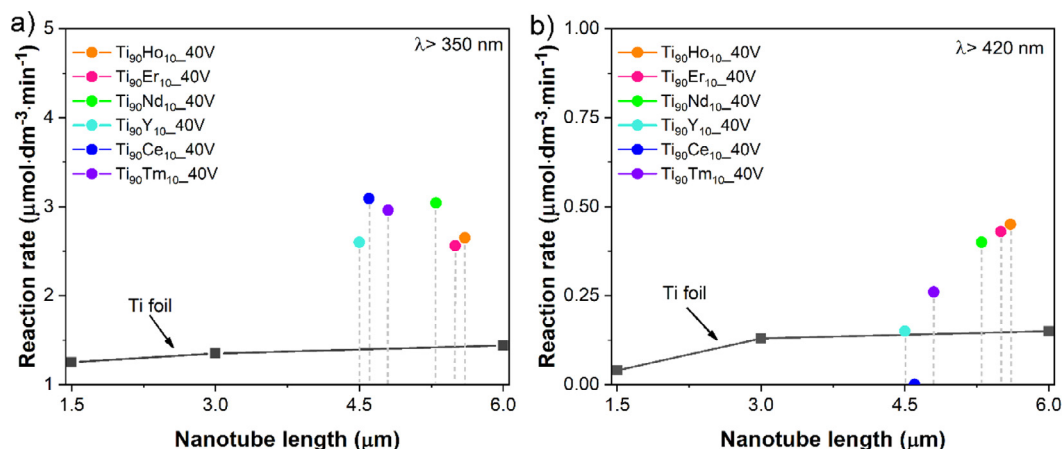
Fig. 8. The correlation between the length and photocatalytic activates of pristine TiO$_2$ NTs and RE-modified TiO$_2$ NTs under (a) UV–Vis ($\lambda > 350$ nm) and (b) Vis ($\lambda > 420$ nm) light irradiation.

nanotube dimensions are responsible for light absorption and the longer the nanotube length, the higher is the light absorption. Based on our previous study, the linear correlation between the length of pristine TiO$_2$ NTs and photocatalytic activity was observed [43]. However, for UV radiation the absorption coefficient increases dramatically, consequently the photogenerated electron has to travel a longer path. In addition, due to the fact that RE metals were found to be on the surface of TiO$_2$ NTs, they lowered the excitation of TiO$_2$. Therefore, it is not always possible to observe correlations. The theoretical kinetic model developed by Liu et al. [69] showed that photocatalytic efficiency increases, till reaches a saturated value as NT length increases, which mainly impacts the change of light absorption as well as the diffusion of reactants along the NTs [69]. The research shows the positive (improved absorption) and negative (longer carrier diffusion path) impact of nanotube length [26,69]. Pasikhani et al. [70] studies were consistent and reported that nanotubes with shorter length (with an optimum of approximately 6.5 μm), exhibited maximum photoactivity in degradation of 2,4-dichlorophenol under UV-assisted irritation. Li et al. [22] reported Er-modified TiO$_2$, synthesised via anodization of titanium in an electrolyte containing ammonium fluoride, ethylene glycol and an erbium precursor, showed 100% photoactivity after 4 h in methylene blue degradation in aqueous phase under UV–Vis (but lower compared to our samples). Moreover, the use of dyes as a model compound for photocatalytic decomposition reaction are not recommended, because of their absorption in the range of visible light and large photo-absorption coefficient [71].

In the case of visible light irradiation (Fig. 8b), the samples showed slightly lower activity compare to UV–Vis irradiation. When holmium was used as modification, the highest reaction rate was observed and equal to 0.45 μmol·dm^{-3}·min^{-1}. In addition, this sample showed stability in four measurement cycles (Fig. 9). This illustrates the high potential of applications. The kinetics of disappearance of phenol followed an apparent first-order rate, therefore the reaction rate decreases with the duration of the process (see Fig. S2 in supplementary material). The intermediate products formed during the phenol photocatalytic degradation under UV–Vis light in presence of pristine and RE-modified TiO$_2$ NTs were consistent with a classic scheme of photodegradation in which the rapid preliminary substrate decomposition was followed by formation of main by-products, such as hydroquinone and benzoquinone (Table S3) [8]. Subsequently, after 20–40 min, the amount of main by-products achieved maximum and then decreased simultaneously with the decrease of the phenol content. These results confirm the behavior observed in photocatalytic performance. The Tm, Nd, Ce-modified TiO$_2$ NTs decrease the amount of primary by-products and hasten their degradation. A high different effect is observed with other samples (Ho, Y, Er-modified TiO$_2$ NTs), the amount of the created
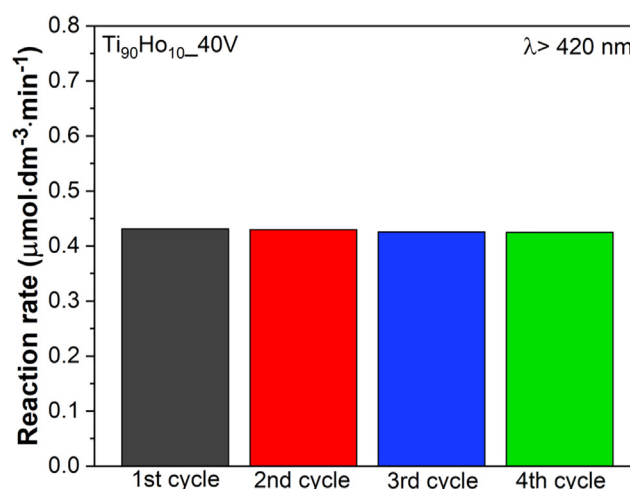

Fig. 9. Phenol degradation rates calculated for the 60 min of visible light ($\lambda > 420$ nm) irradiation in four subsequent degradation cycles.

intermediate products increases, and in the same time, their degradation was slower. Concerning to the intermediate products detected under visible light, the degradation is slower, and it was found that only a low amount of hydroquinone was formed after 1 h (results not shown). It should be noted, that the literature data indicate a more toxic effect of benzoquinone and hydroquinone than phenol [72]. However, the presented studies showed the amount of intermediate products decrease rapidly under the influence of UV–Vis irradiation. In addition, the total organic carbon in the phenol aqueous solution was determined after 7.5 h of photodegradation under visible irradiation in presence of Ho-modified TiO$_2$ NTs. And, it was found that the applied photocatalytic system strives for the formation of carbon dioxide and water (total mineralization), and during that time, approximately 53% of initial phenol was totally mineralized.

At the present time, traditional incandescent lamps are displaced by LEDs in many applications, due to much higher efficiency in light-electricity conversion. In addition, benefits deriving from the implementation of LEDs result from the small dimensions and the long-lasting. Therefore, the research has been extended with photodegradation experiment of toluene in the presence of NTs under the influence of radiation emitted by LEDs with $\lambda_{max} = 375$, 415 and 465 nm and the results are presented in Fig. 10. Under UV LEDs illumination, toluene degradation rate in presence of RE-modified TiO$_2$ NTs reached varies from 5.13×10^{-3} to 5.21×10^{-3} μmol·min^{-1}. However, the efficiency of toluene degradation decreased only to
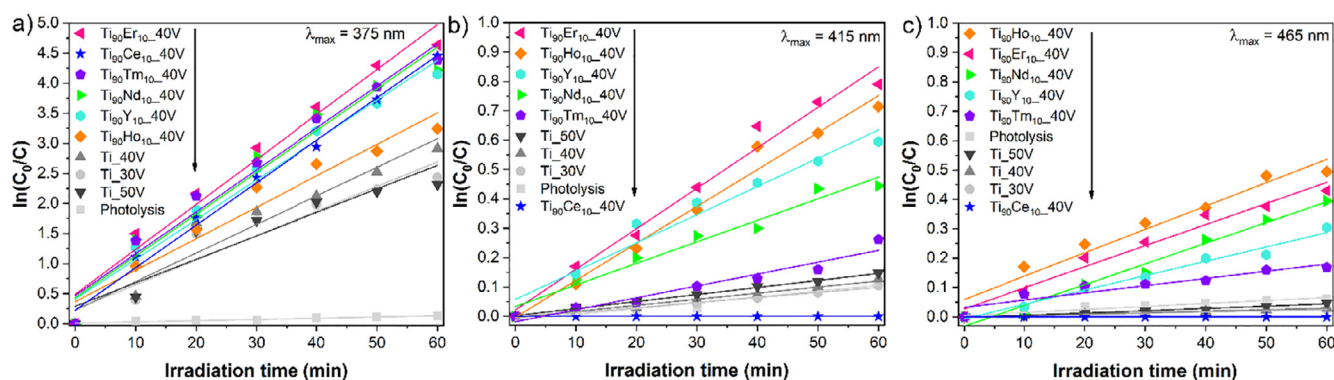
Fig. 10. Linear plot of $\ln(C_0/C)$ for the photodegradation of toluene as a function of LEDs-irradiation time ((a) λ_{max} = 375, (b) λ_{max} = 415 and (c) λ_{max} = 465 nm.) in the presence of pristine and RE-modified TiO_2 NTs.

4.70×10^{-3} µmol·min^{-1} for pristine TiO_2 NTs. The results so obtained point to a clear confirmed that type of RE modification of TiO_2 as well as the larger dimensions of nanotubes slightly improved photoactivity (as discussed in the next section). In case of a longer irradiation wavelength (λ_{max} = 415 nm), lower effectivity of toluene removal (but still relatively high) was obtained, namely the toluene photodegradation rates equaled to 2.85×10^{-3} and 2.87×10^{-3} µmol·min^{-1} for Er- and Ho-TiO_2 NTs (as the most active samples), respectively. Moreover, when the photodegradation experiment of toluene was performed under λ_{max} = 465 nm light irradiation, efficiency decreased to 1.82×10^{-3} and 2.24×10^{-3} µmol·min^{-1}, accordingly. Moreover, visible light induced activity for nanotubes obtained by anodization of $Ti_{90}RE_{10}$ alloys change in order: Ho > Er > Nd > Y > Tm > Ce.

Obregón et al. [73] prepared Er-TiO_2 powder photocatalysts by hydrothermal method and investigated the gas-phase photocatalytic degradation of toluene under UV ($\lambda < 350$ nm) and sunlight (UV content of 3%) irradiation. The toluene photodegradation rates equaled to 2.75 and 1.45 mol·s·m^2 under UV and UV–Vis irradiation, respectively (calculated for the 120 min of irradiation) [73]. However, the drawback of powdered photocatalysts is the problem of separating the photocatalyst after the photocatalytic process, which hinders industrial applications of TiO_2. Obtained results are consistent with our previous study [23], focused on the photocatalytic properties of RE-TiO_2 NTs (RE = Er, Yb, Ho, Tb, Gd, Pr) prepared *via* two-step electrochemical method (preparation of TiO_2 nanotubes by anodic oxidation of Ti followed by electrochemical doping). The holmium-modified sample also showed the highest photoactivity in toluene degradation in gas phase (λ_{max} = 465 nm) in the same reaction conditions. Nevertheless, it was observed the higher photoactivity in present studies, initial reaction rate calculated for the first 10 min of irradiation, increase from 2.5 to 6.16×10^{-3} µmol·min^{-1}. The proposed method allows to obtain photocatalytic surface in one step reaction, thus, it less time-consuming method and avoids generating spend electrolyte containing lanthanide ions [23]. Therefore, the presented research is a promising way to adoption and implementation of the principles of green technology (consisting in minimization of energy and materials input as well as reducing waste generation) [38]. To clarify the interaction between RE ion and the TiO_2 lattice and to probe how this interaction is affected to photocatalytic properties, the plane-wave- based Vienna *ab-initio* simulation package (VASP) implementing spin-polarized density functional theory (DFT) and generalized gradient approximation (GGA) calculations have been employed. Overall, our analysis clearly revealed changes in the structural and energy properties of TiO_2, furthermore, indicated that simultaneous presence of newly formed Ho f states and defects in the TiO_2 surface may contribute to reduction of photon excitation energy and in consequence to the initiation of photoreaction under visible light irradiation [23].

The photocatalytic properties strongly depend on the surface properties, and more specifically on bulk or surface structural defects, because they determine the efficiency by which electrons can be transferred along the long path. Based on XPS analysis, Ti^{3+} and oxygen vacancies are quite common in as-prepared NTs. As a result, the electronic conductivity and optical properties of TiO_2 structures is enhanced (by self-doping) [41,74]. It can be seen that nanotubes formed from $Ti_{90}RE_{10}$ alloys seem to be little prone to oxygen loss and reduction. The RE contents (in at.%) were not compatible with the nominal amount of RE present in the $Ti_{90}RE_{10}$ alloys, because of different chemical properties of them. The samples obtained from $Ti_{90}Ho_{10}$ and $Ti_{90}Er_{10}$ alloys (which showed the highest photoactivity) are characterized by a small content (less than 1 at.%) of the holmium and erbium in TiO_2 NTs. While for other samples, a much larger contribution of RE, may contribute to blocking of the TiO_2 surface, thus causing lowered the excitation of semiconductor. Furthermore, there were observed that when the NTs length increased up to certain optimum, the photoactivity under visible irradiation also increases (see Tables 1 and 4). Based on literature and our previous research, UV-induce photoactivity could be tunable by tubes length, which is affect by applied voltage value during anodic oxidation. On the other hand, Vis-encouraged activity is mostly dependent on the amount of second metal oxide [26,43,69,75,76]. Thus, this point needs more consideration and further research for nanotubes obtained by Ti/RE alloys electrochemical oxidation.

The final stage of studies was monitored which reactive individuals participate in the phenol degradation mechanism under visible ($\lambda > 420$ nm) light irradiation. These studies included a hydroxyl radical test and scavengers test (Fig. 11). The formation of hydroxyl radicals has been monitored following, via spectrophotometric method, using terephthalic acid (TPA). TPA reacts with the photogenerated ·OH radicals forming fluorescent compound (2-hydroxyterephthalic acid). For this reason, the increase of fluorescence (PL) intensity indicates the formation of ·OH radicals. The test was performed irradiating the Ho-modified TiO_2 NTs in TPA solution with visible light and the results are presented in Fig. 11a. Pristine TiO_2 NTs was used as a reference sample.

The fluorescence (PL) spectra intensity increase observed along with exposure time. However, PL spectra of RE-modified TiO_2 exhibited much lower intensity compared with literature data and also almost the same as for TiO_2 NTs [18,77]. The results of this study deny that hydroxyl radicals play a primary role in the photocatalytic process. In order to improve the understanding what type of active species is responsible for photodegradation of pollutants, the trapping experiments with used different reactive species scavengers were performed (Fig. 11b). Ammonium oxalate, benzoquinone, silver nitrate and *tert*-butanol were used as scavengers of h$^+$, O$_2^{·-}$, e$^-$ and ·OH, respectively. The decreased of reaction rate constant indicates the formation of appropriate active species. After addition of ammonium oxalate and *tert*-butanol, similar phenol degradation rate constant were observed compared to the system without scavengers. In contrast to the system containing silver nitrate and benzoquinone, wherein decreased or
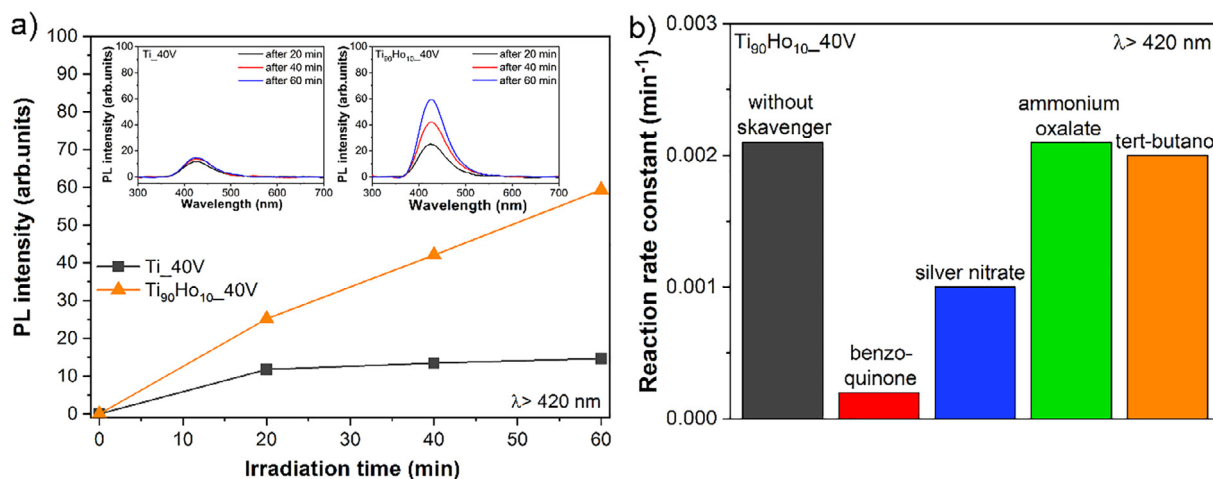
Fig. 11. (a) Fluorescence spectral changes in solution of terephthalic acid under visible ($\lambda > 420$ nm) light irradiation; (b) Phenol degradation rate constant under visible ($\lambda > 420$ nm) light irradiation in the presence of $Ti_{90}Ho_{10}\_40V$ and scavenger.

completely inhibited phenol photodegradation were obtained. Overall, the research suggests that superoxide radical and electrons are the main active species in presented system under visible irradiation, which is consistent with literature reports and our previous research [18,23]. Probably, visible light inducted photoreaction was initiated by the excitation of the RE^{3+}, followed by electrons transfer to the conduction band of TiO_2 NTs. Subsequently, electrons migrate to the surface of the nanotube where they are engaged in the formation of $O_2^{\cdot-}$ and then H_2O_2 and $HO_2^{\cdot}$.

Photoelectrochemical properties

Potential application of the prepared RE-modified TiO_2 NTs and pristine TiO_2 NTs (reference sample) as photoelectrode under visible irradiation was investigated as chronoamperometry and results are displayed in Fig. 12. For all prepared samples, negligible photocurrent was recorded in dark conditions, while the visible irradiation of RE-modified TiO_2 NTs caused a significant increase of photocurrent. Furthermore, no photocurrent was observed in the presence of reference sample (pristine TiO_2 NTs). For all samples, the photocurrent was recorded at 0.5 V bias voltage. Among the RE-modified samples, the measured photocurrent under visible irradiation decreased in the

following order: $Ti_{90}Ho_{10}\_40V$, $Ti_{90}Er_{10}\_40V$, $Ti_{90}Nd_{10}\_40V$, $Ti_{90}Tm_{10}\_40V$, $Ti_{90}Y_{10}\_40V$ $Ti_{90}Ce_{10}\_40V$ (Fig. 12). In this cause, samples modified with Ho, Er, Nd and Tm species exhibited much higher photocurrent generation in comparison with pristine TiO_2 NTs. Photocurrent recorded for $Ti_{90}Ho_{10}\_40V$ was over 10 times higher compared to pristine TiO_2 NTs and 2 times higher than $Ti_{90}Er_{10}\_40V$ (the second most photoactive sample after $Ti_{90}Ho_{10}\_40V$). A direct correlation between photoelectrochemical and photocatalytic activity was observed, which indicates a similar role of TiO_2 modifiers in these processes under visible light (discussed in previous part). An insignificant current was measured for Ti_40V, $Ti_{90}Y_{10}\_40V$ and $Ti_{90}Ce_{10}\_40V$ samples.

Conclusions

It has been demonstrated for the first time that the photocatalytically active, vertically-oriented self-organized nanotubes - made of mixture of TiO_2 and RE_2O_3 – can be formed *via* quite easy and cost-effective one-step electrochemical anodization process of Ti/RE alloy. Contrary to previously reported RE_2O_3-TiO_2 nanotubes, obtained by two step electrochemical method (anodic oxidation of Ti followed by electrochemical doping from electrolyte) [18], currently presented method allows to form photocatalytic surface in one step reaction, which is less time-consuming method and avoids generating spend electrolyte containing lanthanides ions. The presence of RE^{3+} oxides, formed RE-O-Ti boundary of TiO_2 NTs, has been proved using by XRD and XPS analysis. It was observed that the presence of RE strongly affects the photocatalytic ability of TiO_2 NTs, which could be attributed to enhanced absorption range in the visible spectrum as well as enhanced adsorption capacity, and moreover presence of RE *f* states in the band gap of defective TiO_2. Visible light induced activity for nanotubes obtained by anodization of $Ti_{90}RE_{10}$ alloy possesses not only the highest visible light inducted activity, but also stability in four measurement cycles. Moreover, our research indicates that electrons and superoxide radicals play a significant role in the photocatalytic degradation of pollutants. In addition, the photoelectrochemical tests performed under the influence of visible light irradiation confirmed that the RE-modification of TiO_2 NTs caused a significant increase of photocurrent. Photocurrent recorded for $Ti_{90}Ho_{10}\_40V$ (as the most active sample) was over 10 times higher compared to pristine TiO_2 NTs. The present work suggests that nanotubular titanium dioxide modified by rare earth metals can be used as a potential candidate for an environmentally friendly photocatalytic process for the removal of organic pollutants from air and industrial wastewater using irradiation from visible range. Moreover, this type of ordered TiO_2/RE_2O_3 nanotube array could serve as a photocatalytic surface, which could be easily separate from
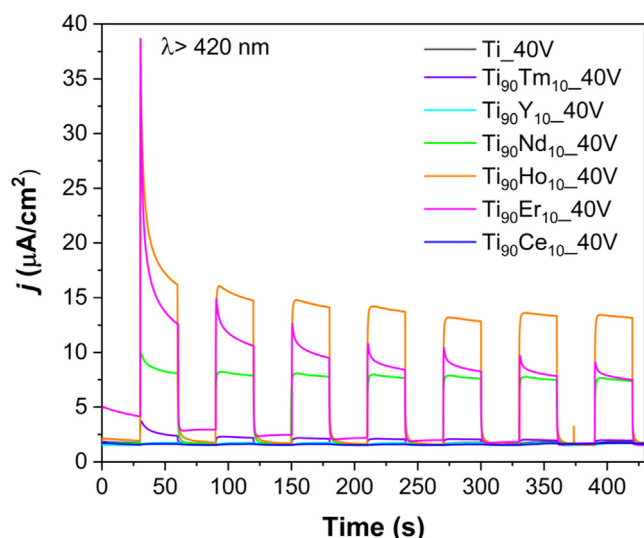

Fig. 12. Transient photocurrent response registered at $+0.5$ V vs. Ag/AgCl/ 0.1 M KCl under visible ($\lambda > 420$ nm) light in the presence of TiO_2 and RE-TiO_2 NTs.

reaction mixture after process and reuse.

Acknowledgements

Appendix A. Supplementary data

Supplementary data to this article can be found online at https://doi.org/10.1016/j.rinp.2018.11.073.

References

[1] Yun J-H, Wang L, Amal R, Ng Y. One-dimensional TiO$_2$ nanostructured photo-anodes: from dye-sensitised solar cells to perovskite solar cells. Energies 2016;9:1030. https://doi.org/10.3390/en9121030.

[2] Reddy NL, Kumar S, Krishnan V, Sathish M, Shankar MV. Multifunctional Cu/Ag quantum dots on TiO$_2$ nanotubes as highly efficient photocatalysts for enhanced solar hydrogen evolution. J Catal 2017;350:226–39. https://doi.org/10.1016/j.jcat.2017.02.032.

[3] Low J, Qiu S, Xu D, Jiang C, Cheng B. Direct evidence and enhancement of surface plasmon resonance effect on Ag-loaded TiO$_2$ nanotube arrays for photocatalytic CO$_2$ reduction. Appl Surf Sci 2018;434:423–32. https://doi.org/10.1016/j.apsusc.2017.10.194.

[4] Zhang J, Xiao G, Xiao F-X, Liu B. Revisiting one-dimensional TiO$_2$ based hybrid heterostructures for heterogeneous photocatalysis: a critical review. Mater Chem Front 2017;1:231–50. https://doi.org/10.1039/C6QM00141F.

[5] Laureys A, Claeys L, De Seranno T, Depover T, Van den Eeckhout E, Petrov R, et al. The role of titanium and vanadium based precipitates on hydrogen induced degradation of ferritic materials. Mater Charact 2018;144:22–34. https://doi.org/10.1016/j.matchar.2018.06.030.

[6] Mirhadi SM, Hassanzadeh Nemati N, Tavangarian F, Daliri Joupari M. Fabrication of hierarchical meso/macroporous TiO$_2$ scaffolds by evaporation-induced self-assembly technique for bone tissue engineering applications. Mater Charact 144 2018:35–41. https://doi.org/10.1016/j.matchar.2018.06.035.

[7] Boyjoo Y, Sun H, Liu J, Pareek VK, Wang S. A review on photocatalysis for air treatment: from catalyst development to reactor design. Chem Eng J 2017;310:537–59. https://doi.org/10.1016/j.cej.2016.06.090.

[8] Nischk M, Mazierski P, Wei Z, Siuzdak K, Kouame NA, Kowalska E, et al. Enhanced photocatalytic, electrochemical and photoelectrochemical properties of TiO$_2$ nanotubes arrays modified with Cu, AgCu and Bi nanoparticles obtained via radiolytic reduction. Appl Surf Sci 2016;387:89–102. https://doi.org/10.1016/j.apsusc.2016.06.066.

[9] Elzarka A, Liu N, Hwang I, Kamal M, Schmuki P. Large-diameter TiO$_2$ nanotubes enable wall engineering with conformal hierarchical decoration and blocking layers for enhanced efficiency in dye-sensitized solar cells (DSSC). Chem – A Eur J 2017;23:12995–9. https://doi.org/10.1002/chem.201702434.

[10] Koo MS, Cho K, Yoon J, Choi W. Photoelectrochemical degradation of organic compounds coupled with molecular hydrogen generation using electrochromic TiO$_2$ nanotube arrays. Environ Sci Technol 2017;51:6590–8. https://doi.org/10.1021/acs.est.7b00774.

[11] Oliveira WF, Arruda IRS, Silva GMM, Machado G, Coelho LCBB, Correia MTS. Functionalization of titanium dioxide nanotubes with biomolecules for biomedical applications. Mater Sci Eng, C 2017;81:597–606. https://doi.org/10.1016/j.msec.2017.08.017.

[12] Khoshnood N, Zamanian A, Massoudi A. Mussel-inspired surface modification of titania nanotubes as a novel drug delivery system. Mater Sci Eng, C 2017;77:748–54. https://doi.org/10.1016/j.msec.2017.03.293.

[13] Terracciano M, Galstyan V, Rea I, Casalino M, De Stefano L, Sbervegleri G. Chemical modification of TiO$_2$ nanotube arrays for label-free optical biosensing applications. Appl Surf Sci 2017;419:235–40. https://doi.org/10.1016/j.apsusc.2017.05.029.

[14] Parnicka P, Mazierski P, Grzyb T, Lisowski W, Kowalska E, Ohtani B, et al. Influence of the preparation method on the photocatalytic activity of Nd-modified TiO$_2$. Beilstein J Nanotechnol 2018;9:447–59. https://doi.org/10.3762/bjnano.9.43.

[15] Wei M, Wan J, Hu Z, Peng Z, Wang B, Wang H. Preparation, characterization and visible-light-driven photocatalytic activity of a novel Fe(III) porphyrin-sensitized TiO2nanotube photocatalyst. Appl Surf Sci 2017;391:267–74. https://doi.org/10.1016/j.apsusc.2016.05.161.

[16] Motola M, Satrapinskyy L, Roch T, Šubrt J, Kupčík J, Klementová M, et al. Anatase TiO$_2$ nanotube arrays and titania films on titanium mesh for photocatalytic NO$_X$ removal and water cleaning. Catal Today 2017;287:59–64. https://doi.org/10.1016/j.cattod.2016.10.011.

[17] Natarajan TS, Natarajan K, Bajaj HC, Tayade RJ. Energy efficient UV-LED source and TiO$_2$ nanotube array-based reactor for photocatalytic application. Ind Eng Chem Res 2011;50:7753–62. https://doi.org/10.1021/ie200493k.

[18] Parnicka P, Mazierski P, Grzyb T, Wei Z, Kowalska E, Ohtani B, et al. Preparation and photocatalytic activity of Nd-modified TiO$_2$ photocatalysts: insight into the excitation mechanism under visible light. J Catal 2017;353:211–22. https://doi.org/10.1016/j.jcat.2017.07.017.

[19] Reszczyńska J, Grzyb T, Wei Z, Klein M, Kowalska E, Ohtani B, et al. Photocatalytic activity and luminescence properties of RE^{3+}-TiO$_2$ nanocrystals prepared by sol-gel and hydrothermal methods. Appl Catal B Environ 2016;181:825–37. https://doi.org/10.1016/j.apcatb.2015.09.001.

[20] Nie J, Mo Y, Zheng B, Yuan H, Xiao D. Electrochemical fabrication of lanthanum-doped TiO$_2$ nanotube array electrode and investigation of its photoelectrochemical capability. Electrochim Acta 2013;90:589–96. https://doi.org/10.1016/j.electacta.2012.12.049.

[21] Fan X, Wan J, Liu E, Sun L, Hu Y, Li H, et al. High-efficiency photoelectrocatalytic hydrogen generation enabled by Ag deposited and Ce doped TiO$_2$ nanotube arrays. Ceram Int 2015;41:5107–16. https://doi.org/10.1016/j.ceramint.2014.12.083.

[22] Li Y, Wang Y, Kong J, Wang J. Synthesis and photocatalytic activity of TiO$_2$ nanotubes co-doped by erbium ions. Appl Surf Sci 2015;328:115–9. https://doi.org/10.1016/j.apsusc.2014.12.054.

[23] Mazierski P, Lisowski W, Grzyb T, Winiarski MJ, Klimczuk T, Mikołajczyk A, et al. Enhanced photocatalytic properties of lanthanide-TiO$_2$ nanotubes: an experimental and theoretical study. Appl Catal B Environ 2017;205:376–85. https://doi.org/10.1016/j.apcatb.2016.12.044.

[24] Shrestha NK, Nah Y-C, Tsuchiya H, Schmuki P. Self-organized nano-tubes of TiO$_2$–MoO$_3$ with enhanced electrochromic properties. Chem Commun (2009) 2008. https://doi.org/10.1039/b820953g.

[25] Aldabergenova SB, Ghicov A, Albu S, Macak JM, Schmuki P. Smooth titania nanotubes: Self-organization and stabilization of anatase phase. J Non Cryst Solids 2008;354:2190–4. https://doi.org/10.1016/j.jnoncrysol.2007.10.037.

[26] Mishra T, Wang L, Hahn R, Schmuki P. In-situ Cr doped anodized TiO$_2$ nanotubes with increased photocurrent response. Electrochim Acta 2014;132:410–5. https://doi.org/10.1016/j.electacta.2014.03.101.

[27] Yasuda K, Schmuki P. Control of morphology and composition of self-organized zirconium titanate nanotubes formed in (NH$_4$)$_2$SO$_4$/NH$_4$F electrolytes. Electrochim Acta 2007;52:4053–61. https://doi.org/10.1016/j.electacta.2006.11.023.

[28] Tsuchiya H, Berger S, Macak JM, Ghicov A, Schmuki P. Self-organized porous and tubular oxide layers on TiAl alloys. Electrochim Commun 2007;9:2397–402. https://doi.org/10.1016/j.elecom.2007.07.013.

[29] Luz AR, Santos LS, Lepienski CM, Kuroda PB, Kuromoto NK. Characterization of the morphology, structure and wettability of phase dependent lamellar and nanotube oxides on anodized Ti-10Nb alloy. Appl Surf Sci 2018;448:30–40. https://doi.org/10.1016/j.apsusc.2018.04.079.

[30] Hang R, Liu Y, Gao A, Zong M, Bai L, Zhang X, et al. Fabrication of Ni-Ti-O nanoporous film on NiTi alloy in ethylene glycol containing NaCl. Surf Coatings Technol 2017;321:136–45. https://doi.org/10.1016/j.surfcoat.2017.04.036.

[31] Yang M, Zhang L, Jin B, Huang L, Gan Y. Enhanced photoelectrochemical properties and water splitting activity of self-ordered MoO$_3$-TiO$_2$ nanotubes. Appl Surf Sci 2016;364:410–5. https://doi.org/10.1016/j.apsusc.2015.12.157.

[32] Ning X, Wang X, Yu X, Li J, Zhao J. Preparation and capacitance properties of Mn-doped TiO$_2$ nanotube arrays by anodisation of Ti-Mn alloy. J Alloy Compd 2016;658:177–82. https://doi.org/10.1016/j.jallcom.2015.10.204.

[33] Roy P, Berger S, Schmuki P. TiO$_2$ nanotubes: synthesis and applications. Angew Chem – Int Ed 2011;50:2904–39. https://doi.org/10.1002/anie.201001374.

[34] Bhethanabotla VC, Russell DR, Kuhn JN. Assessment of mechanisms for enhanced performance of Yb/Er/titania photocatalysts for organic degradation: role of rare earth elements in the titania phase. Appl Catal B Environ 2017;202:156–64. https://doi.org/10.1016/j.apcatb.2016.09.008.

[35] Zhao X, Wu P, Liu M, Lu D, Ming J, Li C, et al. Y$_2$O$_3$ modified TiO$_2$ nanosheets enhanced the photocatalytic removal of 4-chlorophenol and Cr (VI) in sun light. Appl Surf Sci 2017;410:134–44. https://doi.org/10.1016/j.apsusc.2017.03.073.

[36] Touati A, Hammedi T, Najjar W, Ksibi Z, Sayadi S. Photocatalytic degradation of textile wastewater in presence of hydrogen peroxide: Effect of cerium doping titania. J Ind Eng Chem 2016;35:36–44. https://doi.org/10.1016/j.jiec.2015.12.008.

[37] Ye QL, Yang X, Li C, Li Z. Synthesis of UV/NIR photocatalysts by coating TiO2 shell on peanut-like YF$_3$:Yb, Tm upconversion nanocrystals. Mater Lett 2013;106:238–41. https://doi.org/10.1016/j.matlet.2013.05.047.

[38] Anastas J, Zimmerman PT. Design through the twelve principles of green engineering. Env Sci Tech 2003;37:94–101.

[39] Mazierski P, Nadolna J, Lisowski W, Winiarski MJ, Gazda M, Nischk M, et al. Effect of irradiation intensity and initial pollutant concentration on gas phase photocatalytic activity of TiO$_2$ nanotube arrays. Catal Today 2017;284:19–26. https://doi.org/10.1016/j.cattod.2016.09.004.

[40] Sulka GD, Kapusta-Kołodziej J, Brzózka A, Jaskuła M. Anodic growth of TiO$_2$ nanopore arrays at various temperatures. Electrochim Acta 2013;104:526–35. https://doi.org/10.1016/j.electacta.2012.12.121.

[41] Lee K, Mazare A, Schmuki P. One-dimensional titanium dioxide nanomaterials: nanotubes. Chem Rev 2014;114:9385–454. https://doi.org/10.1021/cr500061m.

[42] Hang R, Liu Y, Gao A, Bai L, Huang X, Zhang X, et al. Highly ordered Ni-Ti-O nanotubes for non-enzymatic glucose detection. Mater Sci Eng, C 2015;51:37–42. https://doi.org/10.1016/j.msec.2015.02.027.

[43] Mazierski P, Malankowska A, Kobylański M, Diak M, Kozak M, Winiarski MJ, et al. Photocatalytically active TiO$_2$/Ag$_2$O nanotube arrays interlaced with silver nanoparticles obtained from the one-step anodic oxidation of Ti-Ag alloys. ACS Catal 2017;7:2753–64. https://doi.org/10.1021/acscatal.7b00056.

[44] Khaki MRD, Shafeeyan MS, Raman AAA, Daud WMAW. Application of doped photocatalysts for organic pollutant degradation – a review. J Environ Manage 2017;198:78–94. https://doi.org/10.1016/j.jenvman.2017.04.099.

[45] Ozkan S, Truong N, Mazare A, Cerri I, Schmuki P. Controlled spacing of self-organized anodic TiO$_2$ nanotubes. Electrochem Commun 2016;69:76–9. https://doi.org/10.1016/j.elecom.2016.06.004.

[46] Madian M, Klose M, Jaumann T, Gebert A, Oswald S, Ismail N, et al. Anodically fabricated TiO₂-SnO₂ nanotubes and their application in lithium ion batteries. J Mater Chem A 2016;4:5542–52. https://doi.org/10.1039/c6ta00182c.

[47] Minagar S, Li Y, Berndt CC, Wen C. The influence of titania-zirconia-zirconium titanate nanotube characteristics on osteoblast cell adhesion. Acta Biomater 2015;12:281–9. https://doi.org/10.1016/j.actbio.2014.10.037.

[48] Kim WG, Choe HC, Ko YM, Brantley WA. Nanotube morphology changes for Ti-Zr alloys as Zr content increases. Thin Solid Films 2009;517:5033–7. https://doi.org/10.1016/j.tsf.2009.03.165.

[49] Lai YK, Sun L, Chen C, Nie CG, Zuo J, Lin CJ. Optical and electrical characterization of TiO₂ nanotube arrays on titanium substrate. Appl Surf Sci 2005;252:1101–6. https://doi.org/10.1016/j.apsusc.2005.02.035.

[50] Knorr FJ, Mercado CC, Mchale JL. Trap-state distributions and carrier transport in pure and mixed-phase TiO₂: influence of contacting solvent and interphasial electron transfer. J Phys Chem C 2008;112:12786–94. https://doi.org/10.1021/jp8039934.

[51] Tang H, Berger H, Schmid PE, Levy F. Optical properties of anatase (TiO₂). Pergamon Solid State Commun 1994;92:267–71. https://doi.org/10.1016/0038-1098(94)90889-3.

[52] Zhao H, Pan F, Li Y. A review on the effects of TiO₂ surface point defects on CO₂ photoreduction with H2O. J Mater 2017;3:17–32. https://doi.org/10.1016/j.jmat.2016.12.001.

[53] Regonini D, Bowen CR, Jaroenworaluck A, Stevens R. A review of growth mechanism, structure and crystallinity of anodized TiO₂ nanotubes. Mater Sci Eng R Reports 2013;74:377–406. https://doi.org/10.1016/j.mser.2013.10.001.

[54] Valota A, LeClere DJ, Hashimoto T, Skeldon P, Thompson GE, Berger S, et al. The efficiency of nanotube formation on titanium anodized under voltage and current control in fluoride/glycerol electrolyte. Nanotechnology 2008;19. https://doi.org/10.1088/0957-4484/19/35/355701.

[55] Pfau A, Schierbaum K-D. The electronic structure of stoichiometric and reduced CeO₂ surfaces: an XPS, UPS and HREELS study. Surf Sci 1994;6028. https://doi.org/10.1016/0039-6028(94)90027-2.

[56] Chowdhury S, Lin KS. Characterization and surface reactivity analyses of ceria nanorod catalyst for methanol interaction. Mater Chem Phys 2012;133:163–9. https://doi.org/10.1016/j.matchemphys.2012.01.002.

[57] Armelao L. Plasma-enhanced CVD CeO₂ nanocrystalline thin films analyzed by XPS. Surf Sci Spectra 2001;8:247. https://doi.org/10.1116/11.20020601.

[58] Krawczyk M, Holdynski M, Lisowski W, Sobczak JW, Jablonski A. Electron inelastic mean free paths in cerium dioxide. Appl Surf Sci 2015;341:196–202. https://doi.org/10.1016/j.apsusc.2015.02.177.

[59] Naumkin AV, Kraut-Vass A, Powell CJ, Gaarenstroom SW, National Institute of Standards and Technology (U.S.), NIST X-ray photoelectron spectroscopy database, (2012). http://srdata.nist.gov/xps/Default.aspx.

[60] Yurii AT, Anton Yu T. Structure of X-ray photoelectron spectra of lanthanide compounds. Russ Chem Rev 2002;71:347. https://doi.org/10.1070/RC2002v071n05ABEH000717.

[61] Ulrich MD, Rowe JE, Niu D, Parsons GN. Bonding and structure of ultrathin yttrium oxide films for Si field effect transistor gate dielectric applications. J Vac Sci Technol B Microelectron Nanom Struct 2003;21:1792. https://doi.org/10.1116/1.1593647.

[62] Pan T-M, Lu C-H, Mondal S, Ko F-H. Resistive switching characteristics of Tm₂O₃, Yb₂O₃, and Lu₂O₃-based metal–insulator–metal memory devices. IEEE Trans Nanotechnol 2012;11:1040–6. https://doi.org/10.1109/TNANO.2012.2211893.

[63] Lazăr C, Burzo E, Neumann M. XPS study of RNi₄B compounds, where R = Nd, Tb, Dy, Ho and Er. J Optoelectron Adv Mater 2008;10:780–2.

[64] Reszczyńska J, Grzyb T, Sobczak JW, Lisowski W, Gazda M, Ohtani B, et al. Visible light activity of rare earth metal doped (Er³⁺, Yb³⁺ or Er³⁺/Yb³⁺) titania photocatalysts. Appl Catal B Environ 2015;163:40–9. https://doi.org/10.1016/j.apcatb.2014.07.010.

[65] Cui J, Hope GA, Buckley AN. Spectroscopic investigation of the interaction of hydroxamate with bastnaesite (cerium) and rare earth oxides. Miner Eng 2012;36–38:91–9. https://doi.org/10.1016/j.mineng.2012.03.001.

[66] Wojcieszak APD, Mazur M, Kaczmarek D, Morgiel J, Domaradzki ACJ. Influence of nanocrystalline structure and surface properties of TiO₂: Nd thin films. Pol J Chem Tech 2012;14:1–7. https://doi.org/10.1515/pjct-2015-0047.

[67] Ahmaruzzaman M. Adsorption of phenolic compounds on low-cost adsorbents: a review. Adv Colloid Interface Sci 2008;143:48–67. https://doi.org/10.1016/j.cis.2008.07.002.

[68] Cruz Silvia L, Rivera-García María Teresa, Woodward JJ. Review of toluene action: clinical evidence, animal studies and molecular targets. J Drug Alcohol Res 2014:1–15. https://doi.org/10.4303/jdar/235840.Review.

[69] Liu B, Nakata K, Liu S, Sakai M, Ochiai T, Murakami T, et al. Theoretical kinetic analysis of heterogeneous photocatalysis by TiO₂ nanotube arrays: the effects of nanotube geometry on photocatalytic activity. J Phys Chem C 2012;116:7471–9. https://doi.org/10.1021/jp300481a.

[70] Pasikhani JV, Gilani N, Pirbazari AE. The correlation between structural properties, geometrical features, and photoactivity of freestanding TiO₂ nanotubes in comparative degradation of 2,4-dichlorophenol and methylene blue. Mater Res Express 2018;5:25016. https://doi.org/10.1088/2053-1591/aaaa34.

[71] Ohtani B. Preparing articles on photocatalysis—beyond the illusions, misconceptions, and speculation. Chem Lett 2008;37:216–29. https://doi.org/10.1246/cl.2008.216.

[72] Saylor GL, Chen L, Kupferle MJ. Time varying toxicity of effluents from the electrochemical oxidation of phenol. Procedia Environ Sci 2013;18:451–63. https://doi.org/10.1016/j.proenv.2013.04.061.

[73] Obregón S, Kubacka A, Fernández-García M, Colón G. High-performance Er³⁺-TiO₂ system: dual up-conversion and electronic role of the lanthanide. J Catal 2013;299:298–306. https://doi.org/10.1016/j.jcat.2012.12.021.

[74] Dong G, Wang X, Chen Z, Lu Z. Enhanced photocatalytic activity of vacuum-activated TiO₂ induced by oxygen vacancies. Photochem Photobiol 2018;2. https://doi.org/10.1111/php.12874.

[75] Nevárez-Martínez M, Kobylański M, Mazierski P, Wółkiewicz J, Trykowski G, Malankowska A, et al. Self-organized TiO2–MnO₂ nanotube arrays for efficient photocatalytic degradation of toluene. Molecules 2017;22:564. https://doi.org/10.3390/molecules22040564.

[76] Nevárez-Martínez MC, Mazierski P, Kobylański MP, Szczepańska G, Trykowski G, Malankowska A, et al. Growth, structure, and photocatalytic properties of hierarchical V₂O₅-TiO₂ nanotube arrays obtained from the one-step anodic oxidation of Ti-V alloys. Molecules 2017;22. https://doi.org/10.3390/molecules22040580.

[77] Klein M, Nadolna J, Gołąbiewska A, Mazierski P, Klimczuk T, Remita H, et al. The effect of metal cluster deposition route on structure and photocatalytic activity of mono- and bimetallic nanoparticles supported on TiO₂ by radiolytic method. Appl Surf Sci 2016;378:37–48. https://doi.org/10.1016/j.apsusc.2016.03.191.